2003

Texture analysis of the transition from slip to grain boundary sliding in a continously recrystallized superplastic aluminum alloy

Pérez-Prado, M.T.; McNelley, T.R.; Swisher, D.L.; González-Doncel, G.; Ruano, O.A.

Elsevier

M.T. Pérez-Prado, T.R. McNelley, D.L. Swisher, G. González-Doncel, O.A. Ruano, "Texture analysis of the transition from slip to grain boundary sliding in a continuously recrystallized superplastic aluminum alloy," Materials Science and Engineering, v. A342,(2003), pp. 216-230.
http://hdl.handle.net/10945/55338

ELSEVIER

Materials Science and Engineering A342 (2003) 216–230

MATERIALS SCIENCE & ENGINEERING A

www.elsevier.com/locate/msea

Texture analysis of the transition from slip to grain boundary sliding in a continuously recrystallized superplastic aluminum alloy

M.T. Pérez-Prado [a,b], T.R. McNelley [c,*], D.L. Swisher [c], G. González-Doncel [a], O.A. Ruano [a]

[a] *Departamento de Metalurgia Física, Centro Nacional de Investigaciones Metalúrgicas, C.S.I.C., Avda de Gregorio del Amo 8, 28040 Madrid, Spain*
[b] *Department of Mechanical and Aerospace Engineering, University of California-San Diego, 9500 Gilman Drive, La Jolla, CA 92093-0411, USA*
[c] *Department of Mechanical Engineering, Naval Postgraduate School, 700 Dyer Road, Monterey, CA 93943-5146, USA*

Received 15 March 2002; received in revised form 25 April 2002

Abstract

An investigation was conducted into the phenomenon of continuous recrystallization in a superplastic Al–5%Ca–5%Zn alloy. The as-processed microstructure includes adjacent regions that have lattice orientations corresponding to the symmetric variants of the most prominent texture component, {2 2 5}⟨5 5 4⟩. This orientation is near the copper, or C, component, {1 1 2}⟨1 1 1⟩. A cellular dislocation structure with highly disoriented cell walls was present within these regions. Continuous recrystallization during static annealing resulted in the development of distinct boundaries accompanied by retention and sharpening of the texture and the development of a bimodal grain boundary disorientation distribution. The high-angle boundaries (50–62.8°) are the interfaces between grains having lattice orientations as symmetric variants of the texture, while the low-angle boundaries (2–15°) correspond to a cellular structure within the variants. Such a structure persists during superplastic deformation over a wide range of temperature and strain rate conditions. Both dislocation creep and grain boundary sliding operate simultaneously in response to the applied stress under all testing conditions investigated. The relative contribution of each of these mechanisms varies depending on the testing conditions. This is a consequence of the presence of the variants in the microstructure and their persistence during deformation. Fiber texture formation was not observed during either longitudinal or transverse deformation.

Keywords: Aluminum alloys; Recrystallization and recovery; Grain boundaries; Creep; Superplasticity

1. Introduction

In previous work [1] micro-texture and its evolution during elevated temperature deformation was analyzed for a superplastic 5083 aluminum alloy. This material is representative of alloys for which thermomechanical processing (TMP) includes an overaging treatment followed by severe plastic deformation. Such a TMP results in grain refinement by particle-stimulated nucleation (PSN) of discontinuous, or primary, recrystallization, leading to grain orientations and grain boundary disorientations that are both predominantly random in character. The elevated temperature mechanical behavior of the 5083 alloy was consistent with the predictions of accepted phenomenological models for the independent, additive contributions to the total deformation rate by dislocation creep and grain boundary sliding (GBS) [2–5]. Deformation in the dislocation creep regime was reflected in the formation of a ⟨1 1 1⟩ fiber texture by slip-induced lattice rotation in grains of initially random orientation. The transition from dislocation creep to GBS took place over about an order of magnitude in diffusion-compensated strain rate, and superplastic deformation in the GBS regime resulted in randomizing of texture due to random grain rotations.

Several investigations over a long period of time have provided results for certain superplastic metals that do not conform to such a pattern [6–28]. For example, in some of these alloys deformation texture components that had developed during prior TMP were retained

* Corresponding author. Tel.: +1-831-656-2589; fax: +1-831-656-2238
E-mail address: tmcnelley@nps.navy.mil (T.R. McNelley).

0921-5093/02/$ - see front matter © 2002 Published by Elsevier Science B.V.
PII: S0921-5093(02)00275-7

during superplastic deformation, or other texture components were observed to form. Anisotropy of superplastic deformation has been observed in other materials [6–25]. Furthermore, transmission electron microscopy (TEM) studies have provided evidence of dislocation activity in the form of slip lines that were observed in samples following superplastic deformation [26–28]. These observations have led some authors to suggest that dislocation creep and GBS may contribute jointly and simultaneously to the total strain during superplastic deformation, and do so over a wide range of diffusion-compensated strain rates. This is in distinct contrast to the behavior observed in the superplastic 5083 alloy and to the predictions of phenomenological models that are based on the independent, additive contributions of these mechanisms to the total deformation rate [1].

These observations are common to superplastic aluminum alloys that exhibit continuous recrystallization, either during static annealing or during superplastic straining. The term 'continuous recrystallization' is a phenomenological description for a recovery-dominated microstructural transformation that occurs homogeneously throughout a deformation-induced microstructure in the absence of long-range high-angle boundary migration [29].

In many discussions of superplastic behavior in aluminum alloys, the deformation-induced microstructure at the conclusion of TMP has been envisioned to consist of elongated prior grains that contain cells or subgrains of small disorientation. Several investigators have then suggested that continuous recrystallization consists of a recovery-controlled build up of the average disorientation angle for subgrains within such a structure [30–36]. However, the mechanism of this increase in disorientation is uncertain. It has been attributed to subgrain growth [31], to subgrain coalescence [32], to subgrain rotation [33], to subgrain rotation and switching [34] in a response to the tensile stress, or to the accumulation of dislocations in grain boundaries during elevated temperature deformation [35,36].

A more complex picture of deformation-induced microstructures has emerged in recent investigations of large-strain, low-temperature deformation of pure metals (e.g. [37]). Grain elongation with cell/subgrain formation at small strains gives way as the strain increases to processes of grain subdivision. A classification of resulting boundary types and glossary of terms employed in description of deformation microstructures has recently been provided [37]. At large strains, highly elongated, banded or ribbon-like grain structures are seen to develop. These structures may include large fractions of high-angle boundaries although the initial grain size, the deformation temperature, the solute content and the presence of second-phase particles all strongly influence the resulting structure.

During annealing of such deformation-induced microstructures, recovery processes involving local dislocation rearrangements and short-range boundary migration may lead to the development of a fine grain structure that also comprises a large fraction of high-angle boundaries. In the absence of long-range migration of high-angle grain boundaries these processes would constitute continuous recrystallization. Recent investigations into the behavior of the Al–Ca–Zn alloy [16] of this research and of Supral 2004, an Al–Cu–Zr alloy [38], have examined this perspective on continuous recrystallization using computer-aided electron backscatter diffraction (EBSD) pattern analysis methods. These micro-texture studies have shown that the boundary disorientation distribution in as-processed material is that of a fine, deformation-induced cellular structure. The cell walls likely consist of dislocation arrays of high density due to the severe cold working typical of the final processing stages for such materials. The grain boundary disorientation distributions after annealing corresponded closely to the distribution observed in the cellular structure in the as-processed material. Therefore, it has been suggested that continuous recrystallization during annealing consists mainly of the development of boundaries by evolution of the dislocation arrays of the cell walls. Also, many of the resulting grain boundaries were retained during annealing while others were eliminated, altogether in a manner consistent with retention of the deformation texture.

In the present work, texture and mechanical property data for the Al–5%Ca–5%Zn alloy will be used as an example of a material that exhibits continuous recrystallization. These results suggest a distinctly different pattern of elevated temperature deformation behavior than observed in 5083 aluminum [1]. A model for the deformation-induced microstructure will be introduced and employed to explain this new pattern of behavior.

2. Experimental procedure

The Al–5%Ca–5%Zn alloy was prepared by Alcan, Inc. using aluminum of 99.99% purity. Details of the composition are provided in Table 1. Cast ingots were hot rolled and subsequently cold rolled to a 3.2-mm thick sheet [39].

Tensile tests were performed at various strain rates ranging from 10^{-5} to 10^{-1} s^{-1} at temperatures ranging from 300 to 550 °C (thus including both superplastic

Table 1
Alloy composition (wt.%)

Ca	Zn	Fe	Si	Mg	Al
5.0	4.95	0.18	0.1	0.042	Bal

and non-superplastic conditions). Test coupons were prepared with tensile axes aligned either with the rolling direction (RD) or the transverse direction (TD) of the as-processed sheet. Details of the sample geometry and testing procedure have been given in an earlier report [15]. Tests were also performed to various intermediate strains smaller than the fracture strain. This allowed the evolution of texture with deformation to be followed at all the testing temperatures. Macro- and micro-texture measurements as well as microstructural examination were performed in the mid-layer of the sheet alloy following the procedures given in Ref. [1].

Microstructural observation by TEM was performed in a Phillips EM 400 operating at 120 kV. The Al–5%Ca–5%Zn material was sectioned so that the resulting foil normal would be parallel to the TD of the rolled sheet. Thin foils were prepared in a Struers twin-jet electropolishing apparatus using a solution of nitric acid (20%) and methanol (80%).

Orientation imaging microscopy (OIM) was also employed in this investigation. A thorough introduction to EBSD and OIM has been given by Randle [40]. The electron beam of a scanning electron microscope (SEM), operating in the spot mode, is used as a local orientation probe in OIM on samples of bulk material. System software and hardware (EDAX/TSL) was installed on a Topcon S-510 SEM. In the present work the samples were electropolished with the same nitric acid (20%) and methanol (80%) solution employed for TEM sample preparation. Electron interactions within approximately 50 nm of the sample surface produce Kikuchi patterns on a phosphor screen in the SEM sample chamber. A low-light camera allows these patterns to be captured, analyzed and unambiguously indexed in terms of the Euler angles ϕ_1, Φ and ϕ_2 that describe the local lattice orientation relative to the sample axes. The electron beam is deflected, point-by-point, in raster pattern on the sample surface and the orientation data are acquired and stored along with the location of each point on the sample surface. The point-to-point step size was based on the expected microstructure and size of the region being examined. Data clean-up procedures were employed to ensure that data points with a probability $>$ 95% of correct indexing were retained in the analysis. Individual points having lower probability of correct indexing were re-assigned to neighboring regions of similar orientation. This method was chosen to reduce the effects of pattern overlap in the vicinity of grain boundaries and second-phase particles. The production of grain maps based on the orientation measurements was accomplished by assigning points (pixels) to a grain in regions with orientations differing by less than 2°. The orientation data may also be represented by assigning gray tones to pixels based on quality (sharpness) of the Kikuchi pattern image. Finally, the orientations may also be plotted as discrete pole figures as representations of the micro-texture in the regions of the maps. Various highlighting functions in the software were employed to correlate local lattice orientation as reflected in pole figures to the location of the orientation in the microstructure.

3. Results

Macro- and micro-texture measurements have been previously performed on this Al–5%Ca–5%Zn alloy in the as-received condition as well as after annealing or elevated temperature deformation. [15,16,41]. The X-ray macro-texture results indicated that the as-received material has a weak but definite deformation texture. The most prominent orientation was $\{2\,2\,5\}\langle 5\,5\,4\rangle$, which is located just 5° away from the copper, or C, component, $\{1\,1\,2\}\langle 1\,1\,1\rangle$ [40,41]. The $\{2\,2\,5\}\langle 5\,5\,4\rangle$ component lies close to the β-fiber, which connects the C and the brass, or B, component ($\{0\,1\,1\}\langle 2\,1\,1\rangle$) in Euler space, and therefore is typical of a deformed FCC metal [42]. The micro-texture data were obtained by an interactive EBSD method [16] and also showed the presence of this component in the deformation texture of the as-received material, although a random component was clearly predominant in the texture. The distribution of the grain-to-grain disorientations exhibited a maximum near 45° [16] and appeared to be similar to the Mackenzie distribution for randomly oriented cubes [43]. The OIM data of the present work are consistent with these previous results. Fig. 1 includes OIM results for the as-received microstructure of the Al–5%Ca–5%Zn alloy. Fig. 1a shows a grain color map in which successive orientations were obtained with a step size of 0.2 μm. This map has been plotted to reveal orientation contrast by randomly assigning different colors to (sub)grains having disorientations $\geqslant 2°$; with this resolution the average (sub)grain size is about 0.5 μm. Fig. 1b shows discrete (2 0 0), (2 2 0), and (1 1 1) pole figures, which illustrate a deformation texture as well as a random component. The two symmetric variants of the C-type texture component, ((2 2 5)[5 5 $\bar{4}$] and (2 2 5)[$\bar{5}$ $\bar{5}$ 4]), can be separately distinguished in the orientation measurements and these variants have been highlighted in either red or blue, respectively, in the discrete pole figures. The individual orientation measurements may also be correlated with their corresponding locations in the (sub)grain structure as shown in Fig. 1c. In this representation the data reveal that the microstructure consists of clusters of (sub)grains that belong to each texture variant, as well as intervening regions that correspond to the random component in the pole figures. The latter regions are represented by gray tones based on image quality of the Kikuchi patterns.

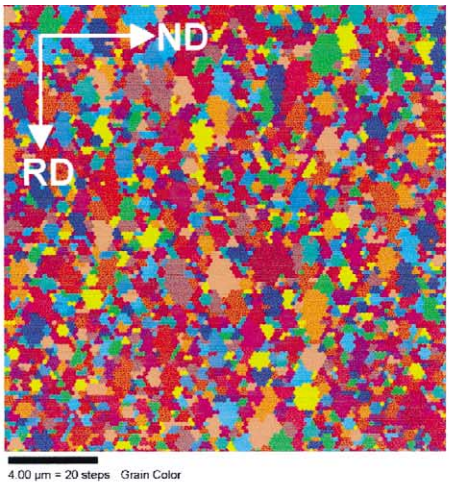

(a)

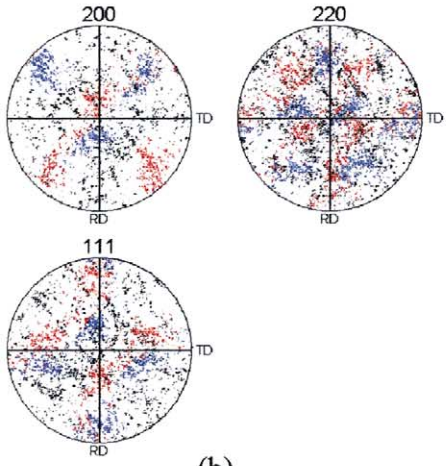

(b)

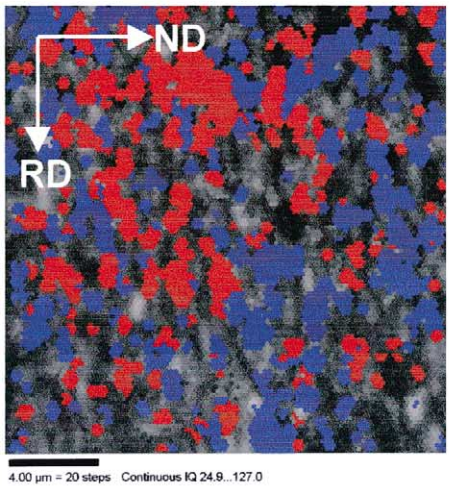

(c)

Fig. 1

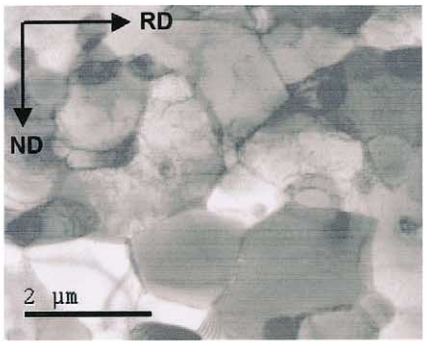

(a)

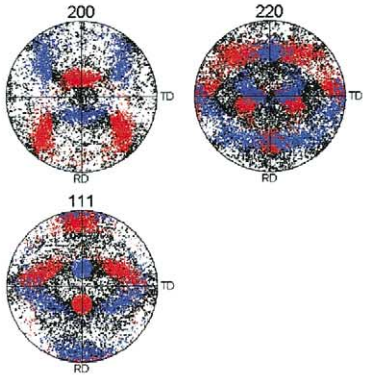

(c)

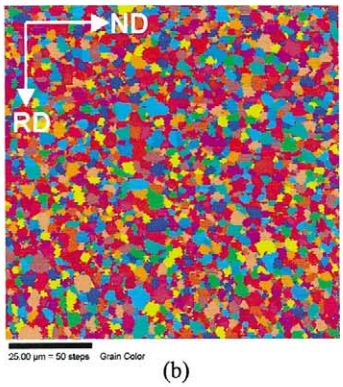

(b)

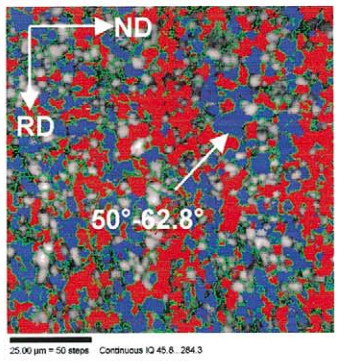

(d)

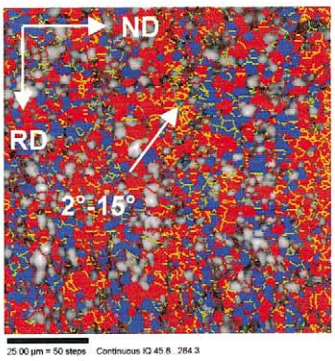

(e)

Fig. 2

The effect of annealing of this alloy at 520 °C has been described in detail previously [16]. It was shown that the weak C-type component observed in the as-received material is retained and progressively strengthened, while the random component is diminished, for annealing times up to 90 h in duration. Simultaneously, the grain size increased. The retention of a deformation texture component during annealing is commonly associated with the phenomenon of continuous recrystallization [30]. A bimodal distribution of the grain-to-grain disorientation angles became apparent after a short annealing time (7 min), with a predominance of either low-angle boundaries, of 2–15° disorientation, or high-angle boundaries, of 50–62.8° disorientation. The bimodal character of the disorientation distribution became increasingly pronounced as the annealing time increased.

The variants of the main texture component, (2 2 5)[5 5 $\bar{4}$] and (2 2 5)[$\bar{5}$ $\bar{5}$ 4]), are related by a rotation of 52° about a ⟨1 1 0⟩ and so it was suggested [16] that the high-angle boundaries in the disorientation distribution separated grains belonging to these variants. Then, it was proposed that the moderately disoriented boundaries separated (sub)grains within each texture variant. Fig. 2 illustrates direct evidence for such a microstructure. The TEM and OIM data presented in this figure were obtained on the RD–ND plane of sample of the Al–5%Ca–5%Zn alloy after 15 min of annealing at 520 °C. Fig. 2a is a TEM micrograph showing a structure with an average (sub)grain size of 2 μm after this short annealing treatment. Distinct, clearly defined boundaries are evident in this TEM image but many poorly-defined, fragmented boundaries can also be observed as well. Fig. 2b is a corresponding OIM grain color map in which (sub)grains disoriented more than 2° or more have been randomly assigned different colors; the apparent (sub)grain size in this grain map is consistent with that observed by TEM. The effective magnification in the grain maps of Fig. 1a and Fig. 2b differ by a factor of five. Thus, microstructural coarsening is rapid in the early stages of annealing at this temperature. Fig. 2c shows the discrete (2 0 0), (2 2 0), and (1 1 1) pole figures, in which orientations located within 15° of the two variants of the C-type texture are again highlighted in either red or blue. The highlighting was accomplished by locating the highest concentration of poles in, for example, the discrete (1 1 1) pole figure and then including all orientations having a {1 1 1} within 15° of the selected location on the pole figure. The number of orientations represented in the pole figures of Fig. 2c is four times that in Fig. 1c and so these discrete pole figures cannot be compared directly. Nevertheless, the texture appears to be somewhat more sharply defined after a 15 min anneal and this is consistent with results obtained in previous studies [16]. Fig. 2d and e are OIM maps of the same region as in Fig. 2b and in which the orientations have been color coded to correspond to the discrete pole figures. In this form these maps illustrate the spatial distribution within the microstructure of these two variant orientations. In contrast to Fig. 1c, it can be seen now, that, after a brief anneal, the microstructure consists almost entirely of clusters of (sub)grains having lattice orientations that correspond to the two variants of the main C-type texture component. Comparison among Fig. 2b, c and d reveals that the clusters of (sub)grains belonging to either of the two variants are irregularly shaped and generally intermingled but also tend to be somewhat elongated and aligned weakly with the RD. Previous investigation of this material [16] had demonstrated the predominance of boundaries disoriented either in the range of 2–15° or 50–62.8° in the annealed microstructure of this material. Highlighting has also been employed in Fig. 2d and e to show the location of the high-angle (Fig. 2d) and low-angle (Fig. 2e) boundaries, respectively. These data document for the first time that the high-angle boundaries (green in Fig. 2d) within such a microstructure separate grains belonging to the two variant orientations, while moderately disoriented boundaries (yellow in Fig. 2e) separate (sub)grains within each variant.

Creep data for this alloy are plotted in Fig. 3 on double logarithmic coordinates as the deformation rate versus the steady state flow stress for tests conducted with the tensile axis parallel to or transverse to the final RD. Separate lines show data for each testing temperature. The slopes of these curves correspond to the stress exponent n, and n values close to 3 were observed when the flow stress was below about 25 MPa, while n values of about 5 were obtained for flow stresses above 25 MPa. Data for the elongation to failure as a function of temperature for two strain rates are plotted in Fig. 4.

Fig. 1. OIM data for the Al–5%Ca–5%Zn alloy in the as-received condition: (a), a random grain color map for (sub)grains disoriented more than 2°; (b), discrete (2 0 0), (2 2 0), and (1 1 1) pole figures in which the two symmetric variants of the main C-type texture component, (2 2 5)[5 5 $\bar{4}$] and (2 2 5)[$\bar{5}$ $\bar{5}$ 4], have been color coded in either blue or red, respectively, using a tolerance of ±15° around the ideal orientations. In (c), the OIM data are re-plotted to show the spatial distribution of (sub)grains oriented as the two symmetric variants of the main texture component.

Fig. 2. OIM data for the Al–5%Ca–5%Zn alloy after annealing at 520 °C for 15 min: (a), a TEM micrograph showing the (sub)grain structure; (b), a random grain color map for (sub)grains disoriented more than 2°; (c), discrete (2 0 0), (2 2 0), and (1 1 1) pole figures in which the two symmetric variants of the main C-type texture component, ((2 2 5)[5 5 $\bar{4}$] and (2 2 5)[$\bar{5}$ $\bar{5}$ 4]), have been colored in blue or red, respectively, using a tolerance of ±15° around the ideal orientations; (d and e), OIM maps showing the spatial distributions of (sub)grains oriented as the two symmetric variants of the main texture component, as well as the location of the high-angle (d) and low-angle boundaries (e), which are highlighted in green or yellow, respectively.

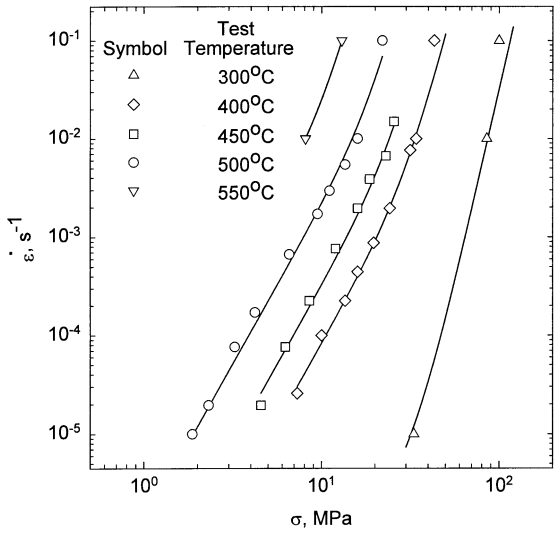

Fig. 3. Creep data for the Al–5%Ca–5%Zn alloy plotted as the logarithm of the steady-state creep rate versus the logarithm of the applied stress for tests conducted with the tensile axes parallel and transverse to the final RD.

The elongation to failure increased with increasing temperature, and reached a maximum of 600% at 550 °C. High values of the elongation to failure were obtained even at strain rates of 10^{-2} s^{-1}, in contrast to the behavior of the 5083 alloy wherein the elongation to failure decreased rapidly with increasing strain rate [1].

No significant texture changes were detected when deforming the Al–5%Ca–5%Zn alloy outside the superplastic regime, at strain rates of 10^{-2} s^{-1} and temperatures lower than 300 °C. The stress exponents then were 5 or higher, and the corresponding elongation to failure values were smaller than 100%. The formation of a fiber texture, which was detected when deforming a discontinuously recrystallized 5083 alloy under dislocation creep conditions [1], was not observed for this Al–5%Ca–5%Zn alloy.

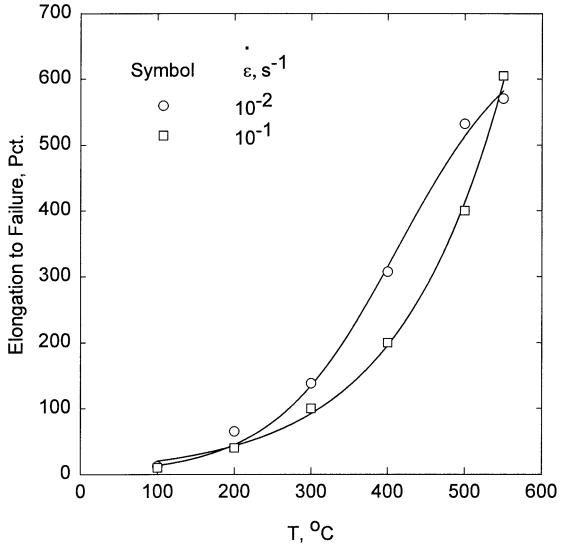

Fig. 4. Elongation to failure data for the Al–5%Ca–5%Zn alloy as a function of temperature for samples deformed at a strain rate of either 10^{-2} or 10^{-1} s^{-1}.

The evolution of the macro-texture of the Al–5%Ca–5%Zn alloy after deformation at high temperatures (400 and 550 °C) is illustrated in Fig. 5a–e. The texture is represented by means of specific $\phi_1 =$ constant sections of the orientation distribution function (ODF). Fig. 5a corresponds to the as-received material. The $\{2\ 2\ 5\}\langle 5\ 5\ 4\rangle$ component is the main texture component and is close to the C orientation, $\{1\ 1\ 2\}\langle 1\ 1\ 1\rangle$. Again, it can be seen that the texture is weak (maximum intensity ≈ 3). The change in the texture of this alloy after tensile deformation at 400 °C and 10^{-2} s^{-1} along either the rolling (RD) or the transverse (TD) direction is illustrated in Fig. 5b or c, respectively. It is important to note that the elongation to failure values achieved under these testing conditions were 200–300%, while the stress exponent n, was close to 5. It can be seen in Fig. 5b that a small lattice rotation during longitudinal tensile extension (parallel to RD) has resulted in a change in the main texture component, from the $\{2\ 2\ 5\}\langle 5\ 5\ 4\rangle$ C-type orientation, to $\{1\ 1\ 2\}\langle 1\ 1\ 1\rangle$, which is the exact C orientation. However, as shown in Fig. 5c, a large rotation during transverse tensile extension (parallel to TD) has resulted in a change in the main texture component from the initial, $\{2\ 2\ 5\}\langle 5\ 5\ 4\rangle$ (C-type) to the $\{0\ 1\ 1\}\langle 2\ 1\ 1\rangle$ B-type texture component [15]. Evidence of fiber texture formation was not seen in the ODF data for these conditions [15]. Nevertheless, the lattice rotations as well as the sharpening of the texture after deformation (maximum intensities of the ODF increase to ~ 7 and 10 for the longitudinal and transverse tests, respectively), are consistent with the predominance of crystallographic slip during deformation for these conditions.

A corresponding study of the texture evolution for the Al–5%Ca–5%Zn alloy deformed under optimum superplastic conditions, at 550 °C and at 10^{-2} s^{-1}, with tensile axis parallel to either the RD or the TD, is depicted in Fig. 5d and e, respectively. The elongation to failure values attained for these conditions were approximately 600% while the stress exponent n, was close to 3. As revealed by comparison of the X-ray results in Fig. 5d and e to those in Fig. 5a there is little apparent change in the $\{2\ 2\ 5\}\langle 5\ 5\ 4\rangle$ C-type texture component following longitudinal extension. A weak B-type component is apparent in the data of Fig. 5e for a sample deformed by transverse tensile deformation. Altogether, the reduction in texture intensity evident in these data is consistent with a large contribution of GBS to the total deformation rate for these testing conditions. Still, the retention of the initial C-type component after longitudinal deformation and the formation of a weak B texture component after transverse deformation suggest

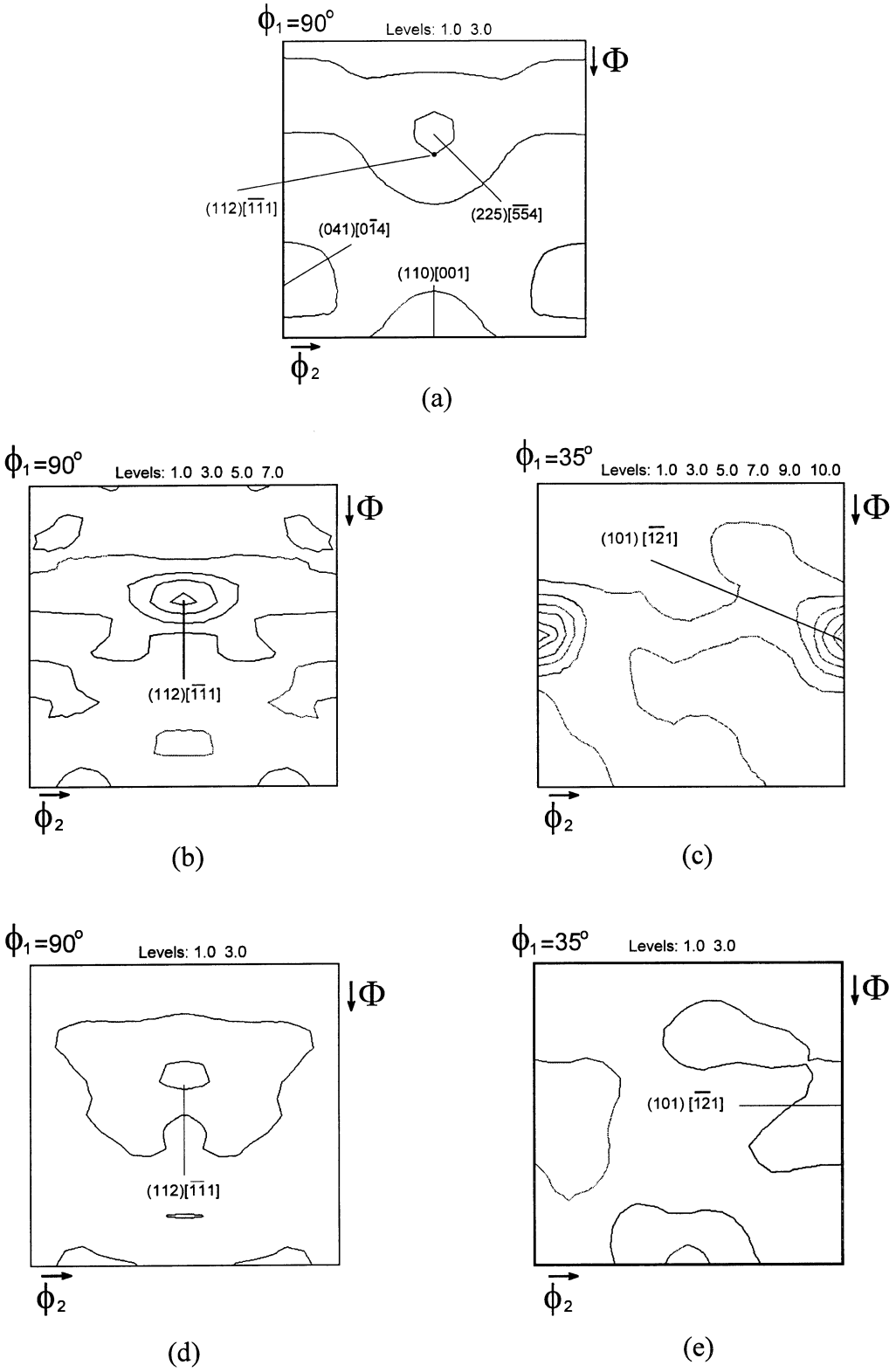

Fig. 5. Macro-texture data for the Al–5%Ca–5%Zn alloy, in the form of specific φ_1 = constant sections of the ODF, illustrating texture evolution during high-temperature deformation. Data in (a), are for the as-received material; (b), corresponds to material deformed at 400 °C/10^{-2} s^{-1} along the *rolling* direction while (c), is for material deformed at 400 °C/10^{-2} s^{-1} along the TD. In (d), data are shown for material deformed at 550 °C/10^{-2} s^{-1} along the *rolling* direction while in (e), data are for material deformed at 400 °C/10^{-2} s^{-1} along the TD.

that crystallographic slip is also contributing to deformation well into the superplastic regime.

Fig. 6 provides OIM data for this alloy following longitudinal tensile deformation at 400 °C and 10^2 s^{-1}, which correspond to the ODF data in Fig. 5b. The OIM grain color map in Fig. 6a illustrates an equiaxed (sub)grain structure. The corresponding micro-texture data is represented in Fig. 6b by means of discrete (2 0 0), (2 2 0), and (1 1 1) pole figures in which the two variants of the main C-type texture component have been highlighted in either red or blue. The grain map in Fig. 6c is for the same region as that in Fig. 6a but now, shows the spatial location of these two symmetric texture variants (in red and blue) as well as the locations of the high-angle boundaries (disorientation of 50–62.8°) in green. Adjacent clusters of (sub)grains belong to the different variants and the clusters now, exhibit elongation along the tensile axis, which is the RD. This map again demonstrates that the high-angle boundaries separate grains belonging to different variants. Fig. 6d is a map of the same region as in Fig. 6a and c now, showing the location in the microstructure of the low-

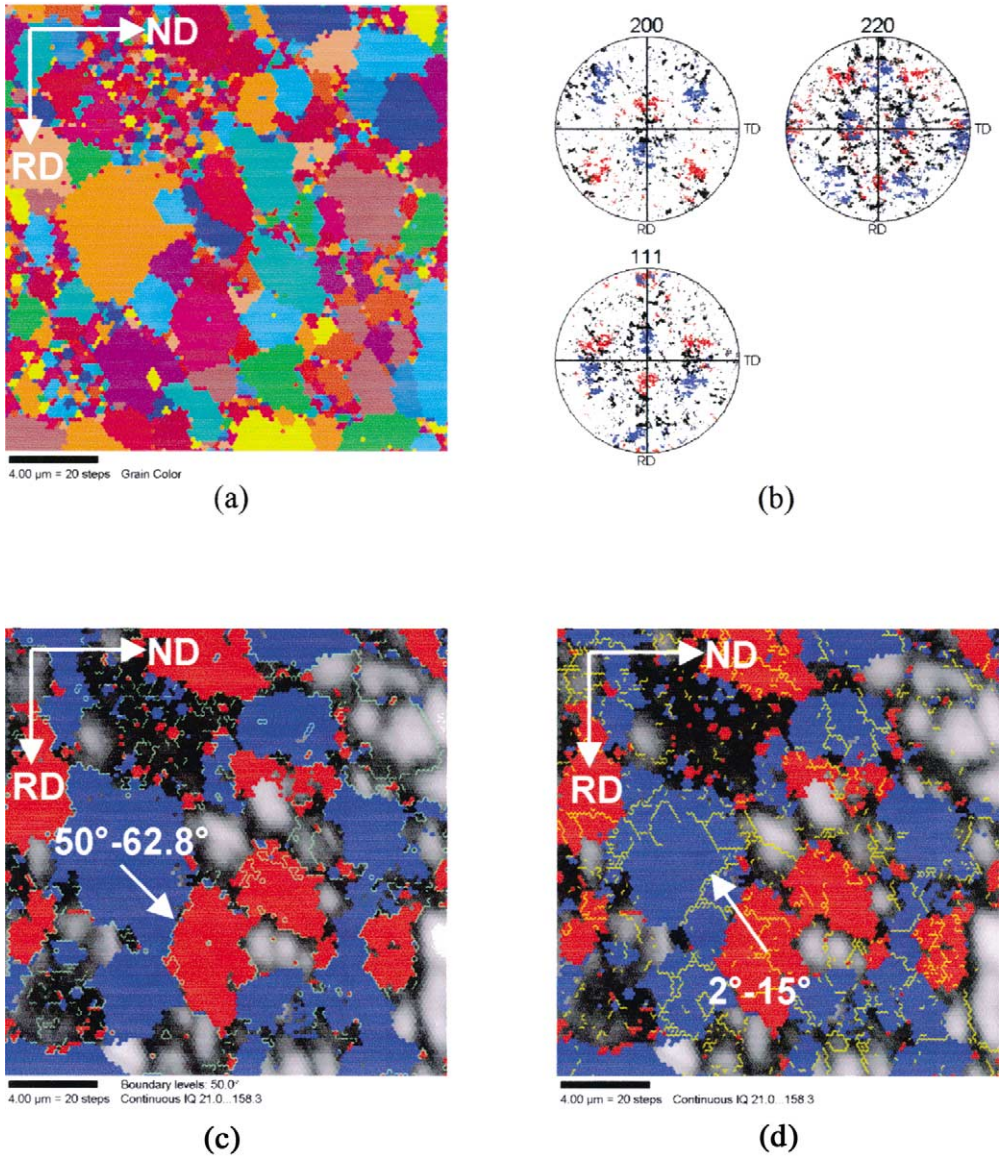

Fig. 6. OIM data for the Al–5%Ca–5%Zn alloy following deformation at 400 °C and 10^{-2} s^{-1} along the *rolling* direction. In (a), a random grain color map is shown to illustrate the (sub)grain structure; in (b), discrete (2 0 0), (2 2 0), and (1 1 1) pole figures have been color coded in either blue or red to highlight the two symmetric variants of the C texture component; (c), shows the same OIM data in the form of map illustrating the spatial distribution of the two symmetric texture variants (also in blue or red) as well as the high-angle boundaries (50–62.8°, in green); (d), is for the same OIM data but now, highlights the low-angle boundaries (2–15°, in yellow).

angle boundaries (disorientation of 2–15°) in yellow. It can be clearly seen here that the low-angle boundaries separate (sub)grains within a cluster.

Fig. 7 provides OIM data for deformation of this Al–5%Ca–5%Zn alloy at 400 °C and 10^{-2} s^{-1} along the TD; these results correspond to the ODF data in Fig. 5c. The grain color map in Fig. 7a illustrates an equiaxed (sub)grain structure following transverse deformation of this material; the structure is similar in appearance to that following longitudinal deformation. The micro-texture after transverse deformation is shown in Fig. 7b by means of discrete (2 0 0), (2 2 0), and (1 1 1) pole figures, which now, indicate the development of a B-type texture component. This change in texture associated with the transverse deformation may be seen most readily by comparing the (1 1 1) pole figure in Fig. 7b to the corresponding (1 1 1) pole figure in Fig. 6b, which had been obtained after longitudinal deformation. The C-type texture in Fig. 6b is marked by a concentration of poles along the RD, while the B-type texture in Fig. 7b is indicated by the development of a concentration of poles along the TD. The B-type texture also has two distinct variants and these have been highlighted in either red or blue. Fig. 7c is OIM map of the same region as in Fig. 7a but which now, shows the spatial location of these two symmetric texture variants (in red

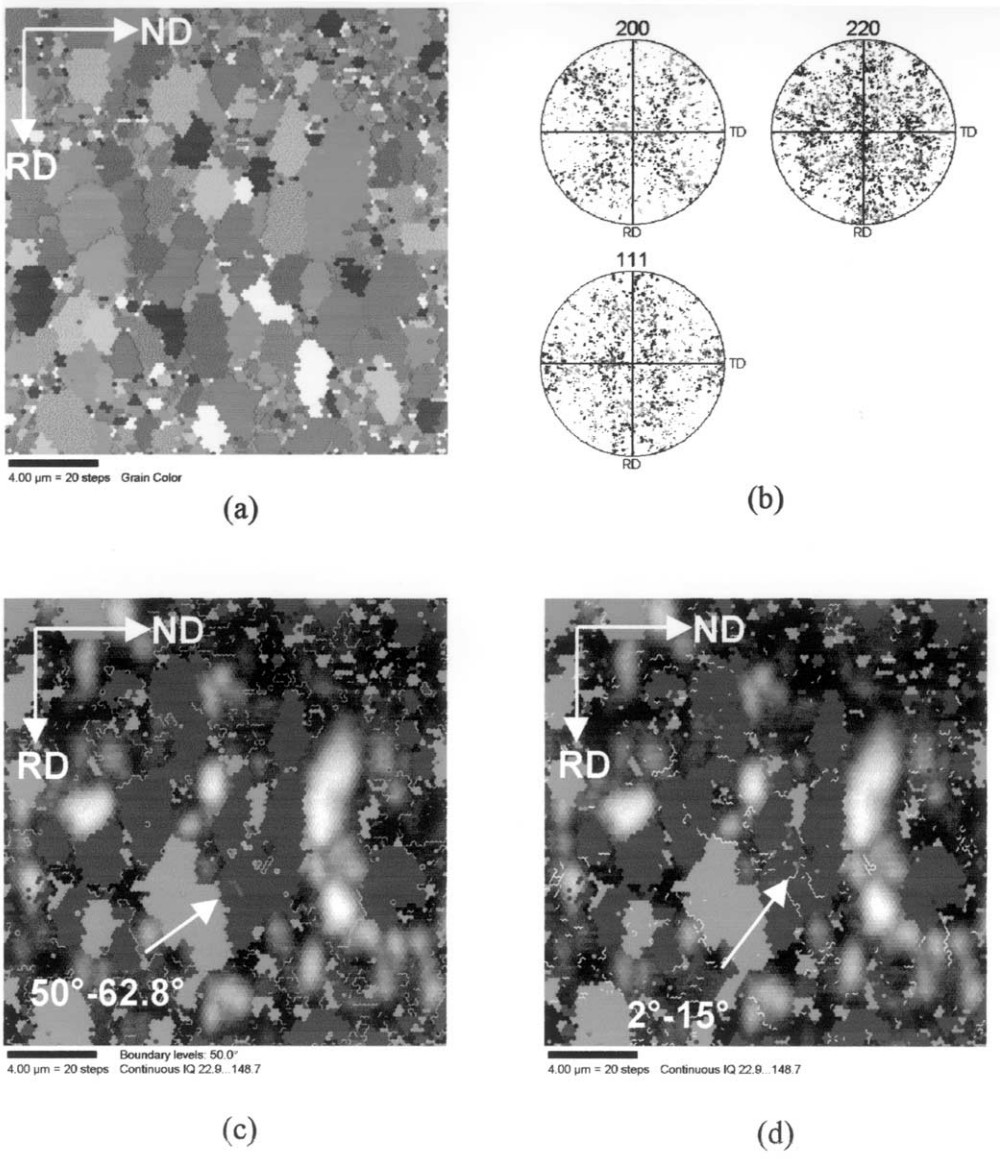

Fig. 7. OIM data for the Al–5%Ca–5%Zn alloy after deformation at 400 °C and 10^{-2} s^{-1} along the TD. In (a), a random grain color map illustrates the (sub)grain structure; in (b), discrete (2 0 0), (2 2 0), and (1 1 1) pole figures have been color coded to highlight the two variants of the main B texture component (compare these data to the pole figures in Fig. 6, wherein a C texture component developed during deformation); (c), shows the same OIM data in the form of a map illustrating the spatial distribution of the two symmetric texture variants (also in blue and red) as well as the high-angle boundaries (50–62.8°, in green); (d), is for the same OIM data but now, the low-angle boundaries are highlighted (2–15°, in yellow).

and blue), as well as the high-angle boundaries (disoriented by 50–62.8°) in green. Again, adjacent clusters of (sub)grains belong to the two variants. These clusters are now, elongated along the TD, which is the tensile axis. Also, the high-angle boundaries separate (sub)grains belonging to different variants. The grain map in Fig. 7d shows the locations of the low-angle boundaries (disoriented by 2–15°) in yellow within the same region as represented in Fig. 7a–c. It can be clearly seen that the low-angle boundaries separate (sub)grains within a cluster belonging to the same texture variant.

4. Discussion

The macro- and micro-texture data and the mechanical response of the Al–5%Ca–5%Zn alloy of this study correlate well with the recognized characteristics of aluminum alloys that transform by a continuous recrystallization reaction. A model for the microstructure must be capable of explaining the development and evolution of the grain boundaries, as well as the grain size and the macro- and micro-texture, during both annealing and elevated temperature deformation. Such a model will be discussed and employed to describe, firstly, the annealing behavior and, subsequently, the elevated temperature deformation characteristics of this alloy.

4.1. Evolution of microstructure during annealing of Al–5%Ca–5%Zn

Altogether, previous studies [15,16] of this Al–5%Ca–5%Zn alloy have clearly shown that the two-phase microstructure of the as-processed material is very fine. The Al_3CaZn second-phase particles are homogeneously distributed, slightly elongated in the RD of the sheet, and about 0.5 μm in length and 0.2 μm in diameter. A cellular substructure, finer than 1 μm in size, is also present. The most prominent component in the texture of the as-processed material is $\{2\ 2\ 5\}\langle 5\ 5\ 4\rangle$, which is very close to the C orientation, a common component of deformation textures of FCC metals. The OIM data obtained for as-processed material in the present study are consistent with these previous results.

The current understanding of the evolution of deformation-induced microstructures is based mainly on studies of severely deformed pure metals [29,37]. Thus, in the initial stages of deformation, subgrains develop and grain subdivision takes place. This is followed by the formation, within the prior grains, of blocks or regions in which lattice rotation takes place in opposite senses. At large strains, a banded, ribbon-like structure may develop in which the prior grain boundaries are no longer readily distinguishable.

Texture development during large-strain deformation by rolling reflects lattice rotation toward stable end orientations. The crystallography of the two C-texture variants is depicted in Fig. 8; the C component is more readily illustrated than $\{2\ 2\ 5\}\langle 5\ 5\ 4\rangle$. Each variant in a C-type texture component has four slip systems with equivalent Schmid factors during plane strain deformation under a Tucker-type stress state ($\sigma_{RD,RD} = -\sigma_{ND,ND}$) [42]. The Schmid factors for all slip systems in both variants are summarized in Table A1 in Appendix A; the four slip systems having equivalent Schmid factors (± 0.544) for this stress state are in conjugate pairs. The incremental strain may be calculated separately for each of the variants in tensor form assuming an identical incremental shear $d\gamma$ on each of these slip systems [1]:

$$d\varepsilon^{C_2} = d\gamma \begin{pmatrix} 1.088 & 0 & -0.962 \\ 0 & 0 & 0 \\ -0.962 & 0 & -1.088 \end{pmatrix}$$

$$d\varepsilon^{C_2} = d\gamma \begin{pmatrix} 1.088 & 0 & 0.962 \\ 0 & 0 & 0 \\ 0.962 & 0 & -1.088 \end{pmatrix}$$

where $d\varepsilon$ is the incremental strain corresponding to $d\gamma$, and C_1 and C_2 refer to the variants (Table A1 in Appendix A). Individually, each variant experiences plane strain deformation with an additional shear term, $\varepsilon_{RD,ND}$ in the strain. Fig. 8 also includes a perspective representation, adapted from Hirsch and Lücke [42], showing an alternating arrangement of elongated bands which have lattice orientation corresponding to the C_1 and C_2 variants. For such an arrangement, averaging of the incremental strains over a region comprising equal volumes of each orientation, as depicted in Fig. 8, would give

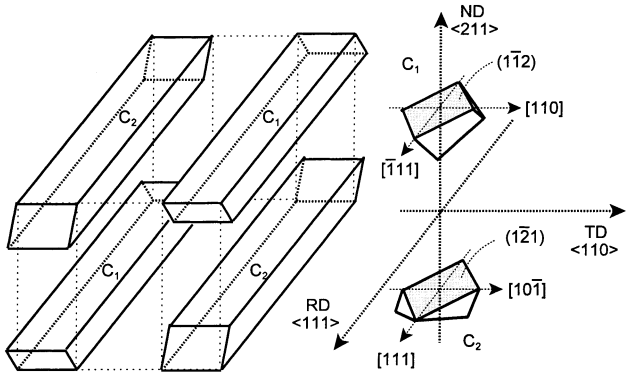

Fig. 8. An idealization of a microstructure formed by alternating bands of lattice orientation corresponding to the symmetric variants of the C texture component, $\{1\ 1\ 2\}\langle 1\ 1\ 1\rangle$, developed during plane strain deformation. The lattice orientations of the variants are illustrated at the right in this diagram.

$$d\varepsilon^{ave} = d\gamma \begin{pmatrix} 1.088 & 0 & 0 \\ 0 & 0 & 0 \\ 0 & 0 & -1.088 \end{pmatrix}$$

i.e. plane strain deformation. Such an arrangement is essentially that predicted by deformation banding models. The potential importance of deformation banding has long been recognized [44,45]. Due to the relaxation of constraints in individual bands, a banded structure is able to deform compatibly with the activation of less than five slip systems in each band [46–48].

Accommodation of the Al_3CaZn second-phase particles during severe plastic deformation would disrupt a tendency to form well-defined bands in the material of this investigation. The presence of such particles, as well as the need to accommodate the additional shears that arise in each band, would be reflected in the development of a cellular structure within the individual bands. In the initial stages of deformation processing the interfaces between adjacent bands may be thick, transitional regions of high dislocation density and lattice curvature, reflecting gradual lattice reorientation from the orientation of one band to that of the next. After more severe deformation such interfaces may become more sharply defined (e.g. [49]). Lattice curvature associated with the interfaces between the bands, with the cellular structure inside of the bands, and with accommodation of the Al_3CaZn particles would account for a large spread of orientations about the main texture component and the appearance of random orientations. This was evident in Fig. 1.

Annealing, particularly at temperatures above 500 °C, has been shown to result in coarsening of the matrix grains, accompanied by coarsening and spheroidization of the Al_3CaZn second-phase particles [16]. Three additional observations lead to the conclusion that a continuous recrystallization reaction occurs during such post-TMP annealing. These were: (a) retention and progressive sharpening of the initial deformation texture; (b), absence of formation of new texture components; and (c), development of a bimodal boundary disorientation distribution, with a high-angle boundary peak at 50–62.8° and a lower-angle peak between 2 and 15° [16]. Coarsening of the matrix grain structure and sharpening of the initial deformation texture during annealing are also evident when Fig. 1 and Fig. 2 are compared. The texture sharpening is consistent with a reduction in lattice curvature, and thus orientation spread about the $\{2\ 2\ 5\}\langle 5\ 5\ 4\rangle$ texture component, due to recovery during the annealing. Following annealing, the microstructure therefore consists mainly of grains of lattice orientations distributed near one or the other of the two distinct variants of this C-type texture component. The highlighting in Fig. 2d clearly shows that the high-angle boundaries (50–62.8°) are the interfaces between regions of lattice orientation near one or the other of the symmetric variants of the $\{2\ 2\ 5\}\langle 5\ 5\ 4\rangle$ texture component, while lower-angle boundaries (2–15°) separate cells within such grains.

Processes of grain subdivision during the prior rolling of this material have resulted in the development of grain clusters of lattice orientation corresponding to the two variants of the $\{2\ 2\ 5\}\langle 5\ 5\ 4\rangle$ texture component. According to the deformation banding model for texture development [44–48], the microstructure would comprise elongated, ribbon-like grains that alternate in lattice orientation. Substructure within such grains would reflect the need for accommodation of the $\varepsilon_{RD,ND}$ shear term and of the Al_3CaZn particles, although the presence of these particles would also disrupt the tendency to form well-defined bands. Thus, the disorientation of the high-angle boundaries in this material became established during the prior deformation processing as a result of grain subdivision and lattice rotation toward the end orientations of the texture variants. The disorientation of the high-angle boundaries is the lattice rotation that relates the variants of the texture (nominally 52° in this material). Cell and substructure formation within the bands during deformation processing then accounts for the disorientation of the lower-angle boundaries. Continuous recrystallization during elevated temperature static annealing of this alloy reflects the recovery-controlled development of the boundaries within the deformation-induced microstructure. These processes would include climb-controlled rearrangement of dense dislocation arrays that separate the adjacent grain clusters, or the cells within clusters, resulting in the evolution of well-defined boundaries in place of the arrays. Grain growth during annealing results in the elimination of many boundaries developed during the prior deformation, but in a manner that maintains the texture in the material. Thus, grains or cells of initial lattice orientation near that of either variant of the texture apparently grow at the expense of nearby regions having lattice orientations in the random population due to lattice curvature associated with a high dislocation density. Such a description of the continuous recrystallization process is consistent with microstructural and microtextural data obtained in an investigation of the annealing response of this alloy [16].

4.2. Elevated temperature mechanical behavior

At the onset of elevated temperature deformation of the superplastic 5083 alloy [1] the microstructure consisted of fine, randomly oriented grains with random, high-angle boundaries. This microstructure had been produced through PSN of discontinuous recrystallization during heating and annealing prior to tensile straining. In contrast, the microstructure of the Al–5%Ca–5%Zn alloy of this study consists of adjacent grain clusters having lattice orientations corresponding

to the symmetric variants of the main texture component. The interfaces that separate the grain clusters as well as those that separate cells within the clusters are deformation-induced boundaries that evolve from dense dislocation arrays by recovery.

An activation energy near that for self-diffusion may be inferred from the data of Fig. 3 and this suggests that lattice self-diffusion controls deformation at the strain rates and temperatures investigated. Constitutive equations for self-diffusion controlled slip creep and GBS processes were presented in Ref. [1] as equations 1–4. Accordingly, the data of Fig. 3 were re-plotted in normalized form as diffusion-compensated strain rate, $\dot{\varepsilon}/D_L$, versus modulus-compensated stress, σ/E. Lattice self-diffusion [50] and dynamic Young's modulus data [51] for pure aluminum were used and the results are presented in Fig. 9. Many pure metals and alloys exhibit power law behavior characterized by a constant n value for $\dot{\varepsilon}/D_L \leqslant 10^{15}$ m^{-2}. Here, the data fall on a single curve but there is a progressive transition from $n=5$ to $n=3$ as diffusion-compensated strain rate, $\dot{\varepsilon}/D_L$, decreases, and superplastic ductility is observed over six orders of magnitude, from $\dot{\varepsilon}/D_L = 10^{14}$ m^{-2} downward to 10^8 m^{-2}. Examination of these data reveals that the transition from $n=5$ to $n=3$ occurs *progressively* over a much wider $\dot{\varepsilon}/D_L$ range than for the 5083 alloy. However, n values for this Al–5%Ca–5%Zn alloy at the extreme values of $\dot{\varepsilon}/D_L$ (10^8 and 10^{14}) are similar to those obtained for the 5083 material [1].

A contribution of dislocation creep to the superplastic response during tensile deformation at $\dot{\varepsilon}/D_L = 5\times10^{13}$ m^{-2} (400 °C and 10^{-2} s^{-1}) is evident in the macro-texture data of Fig. 5. Elongation to failure values of ≈ 300% were accompanied by the development of a distinct *C-type deformation texture* (Fig. 5a and b) by a small lattice rotation from the initial {2 2 5}⟨5 5 4⟩ component, and the *absence of fiber texture formation*.

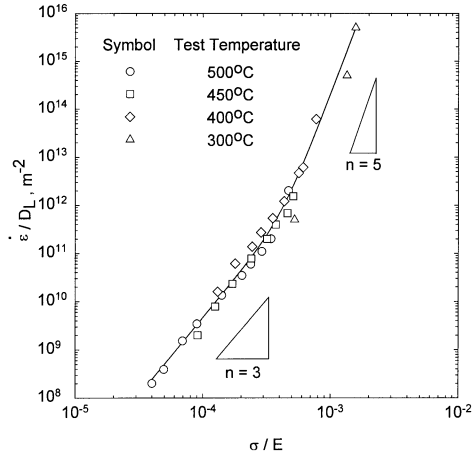

Fig. 9. Diffusion-compensated strain rate as a function of modulus-compensated stress for elevated temperature tension testing of the Al–5%Ca–5%Zn alloy.

This is in distinct contrast to the development of a predominant ⟨1 1 1⟩ fiber texture that was observed in the 5083 alloy when it was deformed under similar conditions involving predominance of dislocation creep. In addition, grain elongation during deformation of the Al–5%Ca–5%Zn alloy [15] was notably less than that observed in 5083 [1]. This is consistent with the simultaneous operation of dislocation creep and GBS mechanisms under these testing conditions.

The C texture component is also apparent in the micro-texture data of Fig. 6b. A ⟨1 1 1⟩ becomes aligned with the tensile axis as lattice rotation to the exact C orientation takes place during tensile extension parallel to the RD. Grains with such a lattice orientation can deform compatibly with their neighbors during dislocation creep and without further lattice rotation. Thus, the C component is a stable end orientation in the texture for uniaxial tension parallel to the RD. The absence of fiber texture formation may be further understood by considering deformation of a FCC crystal along an axis that lays near a ⟨1 1 1⟩ direction, e.g. 5° from such an orientation. It is straightforward to show by means of a stereographic projection that the lattice rotations needed to bring the tensile axis for such a crystal into alignment with the ⟨1 1 1⟩ in question will take place about an axis that is perpendicular to that ⟨1 1 1⟩ and not parallel to it. Thus, such small rotations will have the effect of stabilizing the pre-existing C component but will not produce a fiber texture. The limited extent of grain elongation apparent in the grain map of Fig. 6a is consistent with a contribution of GBS to the total strain, but the high-angle boundaries are still predominantly the interfaces between variant grains.

Deformation at high $\dot{\varepsilon}/D_L$ values of samples with tensile axes parallel to the TD resulted in the development of a distinct *B-type texture component* (ideal orientation is {1 1 0}⟨1 1 2⟩) and, again, the *absence of fiber texture formation*. This is evident in the macro-texture data of Fig. 5c and may also be seen in Fig. 7a–d. The apparent instability of the C component and subsequent lattice rotation resulting in the development of a B texture component during transverse tensile deformation requires further assessment. Calculation of the incremental strains corresponding to incremental shears on the active slip systems in the C component during tensile deformation in the TD may provide further insight into the development of the B texture component. For uniaxial deformation in the TD, the tensile axis tends to align with a ⟨1 1 0⟩ in C-oriented grains (Fig. 8). The Schmid factors for the slip systems in the C component under such a uniaxial stress state are listed in Table A2 of Appendix A, wherein it can be seen that both variants have four slip systems with the highest Schmid factors (±0.408). The incremental strain for equal shears, dα, on each of these four systems would be:

$$d\varepsilon^{C_1} = d\alpha \begin{pmatrix} -0.544 & 0 & 0.769 \\ 0 & 1.633 & 0 \\ 0.769 & 0 & -1.088 \end{pmatrix}$$

$$d\varepsilon^{C_2} = d\alpha \begin{pmatrix} -0.544 & 0 & -0.769 \\ 0 & 1.633 & 0 \\ -0.769 & 0 & -1.088 \end{pmatrix}$$

Averaging over equal volumes of two adjacent variants gives:

$$d\varepsilon^{ave} = d\alpha \begin{pmatrix} -0.544 & 0 & 0 \\ 0 & 1.633 & 0 \\ 0 & 0 & -1.088 \end{pmatrix}$$

which corresponds to uniaxial extension along the TD. However, the R-value, which may be defined as the ratio of the width strain (along RD) to the through-thickness strain (along ND), [52] is not predicted to be unity. This differs from the result for the 5083 alloy and, as well, the result for tensile deformation along the RD of the Al–5%Ca–5%Zn alloy.

The experimental data in Fig. 5c and Fig. 7a–d show that the C component is not stable during transverse deformation, and that lattice rotation results in formation of a B texture component. Detailed analysis of this texture change in previous work [15,16] has shown that the tensile axis rotates along the (0 1 1)–(1 1 1) symmetry boundary of the unit triangle during transverse tensile deformation. It was proposed that this lattice rotation is initiated by slip on two of the four most highly stressed slip systems for the C orientation under transverse tension. As lattice rotation brings a ⟨1 1 1⟩ direction into alignment with the tensile axis (the TD in the B component is a ⟨1 1 1⟩) no further rotation need occur; this is therefore a stable orientation. For uniaxial tension along the TD, the incremental strains for the C orientation when only these two coplanar slip systems operate are:

$$d\varepsilon^{C_1} = d\beta \begin{pmatrix} -0.272 & 0.334 & -0.769 \\ 0.334 & 0.816 & 0.471 \\ -0.769 & 0.471 & -0.544 \end{pmatrix}$$

$$d\varepsilon^{C_2} = d\beta \begin{pmatrix} -0.272 & 0.334 & 0.769 \\ 0.334 & 0.816 & -0.471 \\ 0.769 & -0.471 & -0.544 \end{pmatrix}$$

The average strain tensor over two adjacent variants then becomes:

$$d\varepsilon^{ave} = d\beta \begin{pmatrix} -0.272 & 0.334 & 0 \\ 0.334 & 0.816 & 0 \\ 0 & 0 & -0.544 \end{pmatrix}$$

This would again correspond to a uniaxial tensile deformation along the TD for which the R-value is different from unity. However, there is now, an additional shear term, ε_{12}, the presence of which is reflected in the observed lattice rotation. When the tensile axis reaches the (1 1 1) pole, the resulting B component becomes stable, the shear terms disappear, and the R-value becomes unity.

The exact C orientation with four equally stressed slip systems may reflect a metastable condition when the material is strained in uniaxial tension along the TD. Orientations initially located slightly away from C along the symmetry boundary already have higher Schmid factors for the two coplanar systems above, and therefore would tend to rotate along the symmetry boundary toward B rather than back toward the C orientation.

The large tensile elongations obtained after deformation at high values of $\dot{\varepsilon}/D_L$ (280% at 400 °C/10^{-2} s^{-1}) and retention of an equiaxed grain shape indicates a prominent contribution of GBS in addition to dislocation creep. Grain switching in the absence of grain rotation during GBS along the boundaries between adjacent variants (i.e. the high-angle boundaries) may also allow the retention and stabilization of a texture component.

At low values of $\dot{\varepsilon}/D_L$, where very high tensile elongations (up to 600%) are achieved the stress exponent n, was about 3 for the Al–5%Ca–5%Zn alloy, a value greater than that for the 5083 alloy under GBS-controlled conditions. The maximum tensile ductility was obtained for the sample deformed at $\dot{\varepsilon}/D_L = 10^9$ m^{-2} (550 °C 10^{-2} s^{-1}) and GBS should be the predominant deformation mechanism. In a polycrystalline material, GBS must be accommodated by deformation within the grains; otherwise, voids will form, which may lead to premature failure. Accommodation of GBS by slip involves the generation and short-range motion of dislocations that do not contribute to the total strain [53,54] and, apparently, do not contribute to the development of preferred orientation [1]. Nevertheless, the texture data provide clear indication of slip contributions to the total strain for these conditions. This is especially notable in the texture data for the sample strained in the transverse orientation (Fig. 5e) for which lattice rotation from the initial C orientation to a final B orientation occurred during test. Such a lattice rotation implies that intragranular slip, involving long-range motion of dislocations, is contributing to the total strain for deformation under these conditions in addition to dislocation accommodated GBS. The development of a weak C orientation in the sample deformed parallel to RD is also consistent with this observation.

As the deformation temperature is increased (i.e. $\dot{\varepsilon}/D_L$ decreases), the evolution of the deformation microstructure and development of distinct boundaries should take place more and more rapidly. Unless boundaries are able to support GBS upon initiation of the tension test, dislocation creep processes will predominate and will initiate the same processes of lattice rotation observed in material deformed at high $\dot{\varepsilon}/D_L$ values. This will result in

lattice rotation to the C orientation for testing with the tensile axis parallel to RD, and lattice rotation toward the B orientation for a test with tensile axis parallel to the TD. Concurrent development of distinct boundaries will eventually allow GBS to begin provided that the disorientation distribution includes a sufficient population of boundaries capable of sliding and the grain size remains sufficiently fine for the deformation conditions. Indeed, prior investigation [16] revealed that more than 90% of the boundaries had disorientation angles $>10^{\circ}$ after only 7 min of annealing at 520 °C, and more than $85\% > 10^{\circ}$ after 6 h of annealing at this temperature. In this material the grain size remained <10 μm after 6 h. This emphasizes the need to retard boundary migration; otherwise, excessive grain growth will suppress superplastic response.

Following the onset of GBS, random grain rotation will tend to randomize the texture. The persistence of deformation texture components seen even in samples deformed to failure (with elongation close to 600%) indicates that some grains still remain in a stable orientation while surrounding grains rotate during GBS.

5. Conclusions

Microstructure and texture data corresponding to the Al–5%Ca–5%Zn alloy have been used to exemplify the thermal and mechanical behavior of superplastic alloys in which the microstructure evolves by continuous recrystallization. There are significant differences between the behavior of alloys that transform by continuous recrystallization and those which transform by discontinuous recrystallization.

Grain subdivision during the severe prior rolling deformation leads to the development of adjacent grain clusters having lattice orientations corresponding to the variants of the deformation texture. This may reflect deformation banding during straining, although accommodation of precipitate particles and shears within the bands may preclude the formation of well-defined ribbon-like grains. These accommodation processes apparently lead to the development of a cellular structure within the grain clusters.

Upon annealing the grain clusters retain their identity in the structure. The interfaces between the grain clusters evolve and become the high-angle boundaries in the disorientation distribution. The cell walls within the clusters become the low-angle and moderately disoriented boundaries. Recovery occurs in a manner that preserves the orientation of grain clusters.

This microstructure allows the simultaneous occurrence of dislocation creep and GBS under all the testing conditions investigated. Dislocation creep predominates at small strains because the boundaries are not capable of supporting GBS despite having sufficient disorientation. The evolution of boundary structure occurs more rapidly at lower values of $\dot{\varepsilon}/D_{\mathrm{L}}$ and so the transition from dislocation creep to GBS takes place more readily and GBS predominates over a greater strain interval, leading to greater superplastic ductility. Such alloys are capable of undergoing superplastic deformation at higher strain rates than those that transform by discontinuous recrystallization. This reflects the greater degree of refinement in the former due to retention of the fine scale of the deformation-induced microstructure produced during prior processing and, perhaps, the simultaneous contributions of dislocation creep and GBS to the strain during elevated temperature deformation of such microstructures.

Acknowledgements

This work was supported in part by the Spanish Commission of Science and Technology (CICYT) under grant MAT 97/0700. MPT acknowledges financial support from the Ramóny Cajal program of the Spanish Ministry of Science and Technology.

Appendix A

Table A1. Schmid factors corresponding to a Tucker stress state ($s_{xx} = -s_{zz}$) for each of the 12 slip systems in variants C_1 ((1 $\bar{1}$ 2)[$\bar{1}$ 1 1]) and C_2 ((1 $\bar{2}$ 1)[1 1 1])

Slip plane	Slip direction	Schmid factor	
		C_1	C_2
(1 1 1)	[0 1 $\bar{1}$]	0.408	0
	[$\bar{1}$ 0 1]	0.136	0
	[1 $\bar{1}$ 0]	−0.544	0
($\bar{1}$ $\bar{1}$ 1)	[0 $\bar{1}$ $\bar{1}$]	−0.136	0.136
	[1 0 1]	−0.408	−0.544
	[$\bar{1}$ 1 0]	0.544	0.408
($\bar{1}$ 1 1)	[0 1 $\bar{1}$]	0	−0.408
	[1 0 1]	0	0.544
	[1 $\bar{1}$ 1]	0	−0.136
(1 $\bar{1}$ 1)	[0 $\bar{1}$ $\bar{1}$]	0.544	−0.544
	[$\bar{1}$ 0 1]	−0.544	0
	[1 1 0]	0	0.544

Table A2. Schmid factors corresponding to C_1 ((1 $\bar{1}$ 2)[$\bar{1}$ 1 1]) and C_2 ((1 $\bar{2}$ 1)[1 1 1]) orientations under a tensile stress state in which the tensile axis is parallel to TD

Slip plane	Slip direction	Schmid factor	
		$C1$	$C2$
(1 1 1)	[0 1 $\bar{1}$]	0	0.408
	[$\bar{1}$ 0 1]	0	−0.408
	[1 $\bar{1}$ 0]	0	0
($\bar{1}$ 1 1)	[0 $\bar{1}$ $\bar{1}$]	−0.408	0.408
	[1 0 1]	0	−0.408
	[$\bar{1}$ 1 0]	0.408	0
(1 1 1)	[0 1 $\bar{1}$]	−0.408	0
	[1 0 1]	0	0
	[$\bar{1}$ $\bar{1}$ 0]	0.408	0
(1 $\bar{1}$ 1)	[0 1 $\bar{1}$]	0	0
	[$\bar{1}$ 0 1]	0	0
	[1 1 0]	0	0

References

[1] M.T. Pérez-Prado, G. González-Doncel, O.A. Ruano, T.R. McNelley, Acta Mater. 49 (2001) 2259.
[2] O.D. Sherby, J. Wadsworth, Prog. Mater. Sci. 33 (1989) 166.
[3] O.A. Kaibyshev, Superplasticity of Alloys, Intermetallics and Ceramics, Springer, Berlin, Germany, 1992.
[4] A.H. Chokshi, A.K. Mukherjee, T.G. Langdon, Mater. Sci. Eng. R 10 (1993) 237.
[5] T.G. Nieh, J. Wadsworth, O.D. Sherby, Superplasticity in Metals and Ceramics, Cambridge University Press, Cambridge, UK, 1997.
[6] J.W. Edington, K.N. Melton, C.P. Cutler, Prog. Mater. Sci. 21 (1976) 63.
[7] O.A. Kaibyshev, B.V. Rodionov, R.Z. Valiev, Acta Metall. 26 (1978) 1877.
[8] O.A. Kaibyshev, I.V. Kazachkov, R.M. Galeev, J. Mater. Sci. 16 (1981) 2501.
[9] K. Matsuki, H. Morita, M. Yamada, Y. Murakami, Met. Sci. 6 (1977) 156.
[10] C.P. Cutler, J.W. Edington, J.S. Kallend, K.N. Melton, Acta Metall. 22 (1974) 665.
[11] K.N. Melton, J.W. Edington, Scripta Metall. 8 (1974) 1141.
[12] R.H. Bricknell, J.W. Edington, Acta Metall. 27 (1979) 1303.
[13] R.H. Bricknell, J.W. Edington, Acta Metall. 27 (1979) 1313.
[14] K.N. Melton, J.W. Edington, J.S. Kallend, C.P. Cutler, Acta Metall. 22 (1974) 165.
[15] M.T. Pérez-Prado, M.C. Cristina, O.A. Ruano, G. González-Doncel, Mater. Sci. Eng. 244 (1998) 216.
[16] M.T. Pérez-Prado, T.R. McNelley, O.A. Ruano, G. González-Doncel, Metall. Trans. A 29A (1998) 485.
[17] K. Tsuzaki, H. Matsuyama, M. Nagao, T. Maki, Mater. Trans. JIM 31 (1990) 983.
[18] L. Qing, H. Xiaoxu, Y. Mei, Y. Jinfeng, Acta Mater. 40 (1992) 1753.
[19] J. Liu, D.J. Chakrabarti, Acta Mater. 44 (1996) 4647.
[20] P.L. Blackwell, P.S. Bate, Metall. Trans. A 24A (1993) 1085.
[21] P.S. Bate, Metall. Trans. A 23A (1992) 1467.
[22] P.L. Blackwell, P.S. Bate, in: N. Ridley (Ed.), Superplasticity: 60 Years after Pearson, The Institute of Materials, Manchester, UK, 1994, p. 183.
[23] R.H. Johnson, C.M. Parker, L. Anderson, O.D. Sherby, Phil. Mag. 18 (1968) 1309.
[24] N. Naziri, R. Pearce, J. Inst. Met. 98 (1970) 71.
[25] D.S. McDarmaid, A.W. Bowen, P.G. Partridge, Mater. Sci. Eng. A 64 (1984) 105.
[26] L.C.A. Samuelsson, K.N. Melton, J.W. Edington, Acta Metall. 24 (1976) 1017.
[27] B.P. Kashyap, A. Arieli, A.K. Mukherjee, J. Mater. Sci. 20 (1985) 2661.
[28] L.K.L. Falk, P.R. Howell, G.L. Dunlop, T.G. Langdon, Acta Metall. 34 (1986) 1203.
[29] F.J. Humphreys, Acta Mater. 45 (1997) 5031.
[30] R.D. Doherty, D.A. Hughes, F.J. Humphreys, J.J. Jonas, D. Juul Jensen, M.E. Kassner, W.E. King, T.R. McNelley, H.J. McQueen, A.D. Rollet, Mater. Sci. Eng. A 238/2 (1997) 219.
[31] E. Nes, in: B. Baudelet, M. Suèry (Eds.), Superplasticité, Centre National de la Recherche Scientifique, París, 1985, p. 71.
[32] E. Hornbogen, Metall. Trans. A 10A (1979) 947.
[33] H. Gudmundsson, D. Brooks, J.A. Wert, Acta Mater. 39 (1991) 19.
[34] M.T. Lyttle, J.A. Wert, J. Mat. Sci. 29 (1994) 3342.
[35] S.J. Hales, T.R. McNelley, H.J. McQueen, Metall. Trans. A 22A (1991) 1037.
[36] K. Tsuzaki, H. Xiaoxu, T. Maki, Acta Mater. 44 (11) (1996) 4491.
[37] D.A. Hughes, N. Hansen, Acta Mater. 45 (1997) 3871.
[38] T.R. McNelley, M.E. McMahon, M.T. Pérez-Prado, Phil. Trans. Roy. Soc. A 357 (1999) 1683.
[39] D.M. Moore, L.R. Morris, Mater. Sci. Eng. 43 (1980) 85.
[40] V. Randle, Microtexture Determination and Its Applications, The Institute of Metals, 1992.
[41] M.T. Pérez-Prado, M.C. Cristina, O.A. Ruano, G. González-Doncel, J. Mater. Sci. 32 (1997) 1313.
[42] J. Hirsch, K. Lücke, Acta Metall. 36 (1988) 2883.
[43] J.K. Mackenzie, Biometrica 45 (1958) 229.
[44] C.S. Barrett, Trans. Am. Inst. Min. Engrs. 135 (1939) 296.
[45] C.S. Barrett, H. Levenson, Trans. Am. Inst. Min. Engrs. 137 (1940) 327.
[46] C.S. Lee, B.J. Duggan, Acta Metall. Mater. 41 (1993) 2691.
[47] C.S. Lee, B.J. Duggan, R.E. Smallman, Acta Metall. Mater. 41 (1993) 2265.
[48] K. Kulkarni, E.A. Starke, Jr., D. Kuhlmann-Wilsdorf, Acta Mater. 46 (1998) 5283.
[49] P. Wagner, O. Engler, K. Lücke, Acta Metall. Mater. 43 (1995) 3799.
[50] T.S. Lundy, J.F. Murdock, J. Appl. Phys. 33 (1962) 1671.
[51] W. Köster, Z. Metallk. 89 (1948) 1.
[52] U.F. Kocks, C.N. Tomé, H.R. Wenk, Texture and Anisotropy, Cambridge University Press, 1998, p. 427.
[53] T.G. Langdon, Metall. Mater. Trans. 33 (2002) 49.
[54] R.Z. Valiev, T.G. Langdon, Acta Metall. 41 (1993) 949.